

Anomalous Hall Effect in Polycrystalline Mn_xSi_{1-x} ($x \approx 0.5$) Films with the Self-Organized Distribution of Crystallites over Their Shapes and Sizes

Chernoglazov, K. Y.; Nikolaev, S. N.; Rylkov, V. V.; Semisalova, A. S.; Zenkevich, A. V.; Tugushev, V. V.; Vasil'Ev, A. L.; Chesnokov, Y. M.; Pashaev, E. M.; Matveev, Y. A.; Granovskii, A. B.; Novodvorskii, O. A.; Vedeneev, A. S.; Bugaev, A. S.; Drachenko, O.; Zhou, S.;

Originally published:

June 2016

JETP Letters 103(2016)7, 476-483

DOI: <https://doi.org/10.1134/S0021364016070055>

Perma-Link to Publication Repository of HZDR:

<https://www.hzdr.de/publications/Publ-23775>

Release of the secondary publication
on the basis of the German Copyright Law § 38 Section 4.

Anomalous Hall Effect in Polycrystalline $\text{Mn}_x\text{Si}_{1-x}$ ($x \approx 0.5$) Films with the Self-Organized Distribution of Crystallites over Their Shapes and Sizes

K. Yu. Chernoglazov^a, S. N. Nikolaev^a, V. V. Rylkov^{a,f,*}, A. S. Semisalova^{b,c},
A. V. Zenkevich^d, V. V. Tugushev^a, A. L. Vasil'ev^a, Yu. M. Chesnokov^a, E. M. Pashaev^a,
Yu. A. Matveev^d, A. B. Granovskii^b, O. A. Novodvorskii^e, A. S. Vedenev^f,
A. S. Bugaev^{d,f}, O. Drachenko^g, and S. Zhou^c

^a National Research Centre Kurchatov Institute, pl. Kurchatova 1, Moscow, 123182 Russia

^b Lomonosov Moscow State University, Moscow, 119991 Russia

^c Helmholtz-Zentrum Dresden-Rossendorf, Institute of Ion Beam Physics and Materials Research, Dresden, 01328 Germany

^d Moscow Institute of Physics and Technology, Institutskii per. 9, Dolgoprudnyi, Moscow region, 141700 Russia

^e Institute on Laser and Information Technologies, Russian Academy of Sciences, Svyatoozerskaya ul. 1, Shatura, Moscow region, 140700 Russia

^f Kotelnikov Institute of Radio Engineering and Electronics, Russian Academy of Sciences, Fryazino Branch, pl. Vvedenskogo 1, Fryazino, Moscow region, 141190 Russia

^g Laboratoire National des Champs Magnétiques Intenses, UPR 3228, CNRS-UJF-UPS-INSA, avenue de Ranguel 143, Toulouse, 31400 France

* e-mail: vvrylkov@mail.ru

Received February 9, 2016; in final form, February 24, 2016

The structural, transport, and magnetic characteristics of polycrystalline $\text{Mn}_x\text{Si}_{1-x}$ ($x \approx 0.51$ – 0.52) films grown by pulsed laser deposition onto $\text{Al}_2\text{O}_3(0001)$ substrates when the low-energy components are deposited owing to collisions with the atoms of the buffer gas have been studied in the “shadow” geometry. The magnetization of these films is determined by two ferromagnetic phases—the high-temperature phase with the Curie temperature $T_C \approx 370$ K and the low-temperature one with $T_C \approx 46$ K. The anomalous Hall effect changes sign from positive to negative with a decrease in temperature. The sign change occurs in the temperature range of 30–50 K; the specific value of this temperature depends on the thickness of the $\text{Mn}_x\text{Si}_{1-x}$ film. The results can be interpreted in terms of the structural self-organization related to the formation of two layers in the course of film growth. These layers have nearly the same chemical composition but significantly differ in the shapes and sizes of crystallites. This leads to a drastic difference in the values of T_C and in the value and the sign of the anomalous Hall effect for such layers.

1. The anomalous Hall effect (AHE) is a complex quantum phenomenon discovered in 1880, was first explained in 1954 [1], and is still actively studied experimentally and theoretically [2–14]. This effect is determined by the spin–orbit coupling and by the spin polarization of charge carriers. It is the most clearly pronounced in magnetic materials (ferromagnetic metals and semiconductors, granular metal–insulator nanocomposites, etc.). Their Hall resistivity is described by the sum of two terms

$$R_H = \frac{R_0}{d} B + \frac{R_s}{d} M = R_H^n + R_H^a, \quad (1)$$

where d is the thickness of the magnetic material layer, R_0 is the constant of the normal Hall effect caused by the Lorentz force, B is the magnetic field, R_s is the constant of the anomalous Hall effect caused by the influence of the spin–orbit coupling on the transport of spin-polarized current carriers, M is the magnetization, and $R_H^n = \rho_H^n/d$ and $R_H^a = \rho_H^a/d$ are the components of resistivity corresponding to the normal and anomalous Hall effect, respectively.

One of the most interesting lines in research of the AHE is the study of the relation between the anomalous component of the Hall resistivity ρ_H^a and the lon-

gitudinal resistivity $\rho_{xx} = \rho$ manifesting itself as a so-called scaling behavior, $\rho_H^a \propto \rho^\alpha$, where α is the exponent determined by the physical mechanism underlying the AHE [2, 4–13]. The AHE mechanisms include extrinsic mechanisms related to the spin-dependent scattering of charge carriers by defects in the crystal [15, 16] and the intrinsic mechanism [1] determined by the Berry curvature and the topological characteristics of the Bloch states in the spin subbands affected by the spin–orbit coupling [17, 18]. In metallic systems, at the elastic scattering of charge carriers (low temperatures), $\alpha = 1$ for the skew scattering mechanism [15] of the AHE and $\alpha = 2$ for the side-jump [16] and intrinsic [1, 17, 18] mechanisms. Currently, the scaling is often expressed in terms of the Hall conductivity $\sigma_H^a = \rho_H^a / \rho^2 = \rho_H^a \sigma^2$. According to such representation, $\sigma_H^a \propto \sigma$ for the skew scattering mechanism and $\sigma_H^a = \text{const}$ for the side-jump and intrinsic mechanisms of AHE. Strictly speaking, the aforementioned classification of AHE mechanisms is inapplicable for strongly disordered conductors (in particular, for magnetic semiconductors and metallic materials with a low conductivity, $\sigma < 10^4 \Omega^{-1} \text{cm}^{-1}$). These materials exhibit another type of scaling, $\sigma_H^a \propto \sigma^\gamma$ with $\gamma \approx 1.6$, which was quite recently reported in [5, 19–21]. Such scaling (with $\gamma = 1.4–1.6$) was also observed in metal–insulator nanocomposites near the percolation threshold, including that at the insulator side of the threshold in the regime of hopping conductivity [8, 12, 22]. In the case of the systems with metallic conductivity, it is attributed to the suppression of the intrinsic AHE mechanism owing to the strong scattering of charge carriers [23]. The aforementioned scaling types are observed when the longitudinal electrical resistivity varies owing to the changes in the degree of disorder (in the concentration of magnetic impurities, fluctuations of the potential, etc.) and in temperature. In the latter case, the inelastic scattering of electrons by phonons and/or by magnons can play a significant role and drastically modify the scaling [4, 6, 7, 13, 24].

Another unusual case of deviation from the conventional scaling types takes place when the sign of the AHE changes with the decrease in temperature while the sign of the normal Hall effect remains the same [5, 10, 11, 24–26]. As a rule, the physical mechanism underlying the change of sign is discussed at a qualitative level since this phenomenon is caused in general by different factors such as specific features of the band structure in a given material, position of the Fermi level, relative orientation of orbital and spin moments, and type of scattering potential (repulsive or attractive) [27]. In particular, these factors can cause the difference in sign between the AHE and the normal Hall effect. For example, the sign of the AHE is positive in Fe, but is negative in Ni. Most often, the change in the sign of the AHE is attributed either to

the features of the electron density of states at the Fermi level and the change in its position with temperature [5, 25, 26] or to the competition of the temperature-dependent mechanisms determining the sign of the AHE [10, 11, 24].

In this work, we reveal the change in the sign of the AHE in nonstoichiometric $\text{Mn}_x\text{Si}_{1-x}$ ($x \approx 0.51–0.52$) films, in which we earlier observed the high-temperature ferromagnetism accompanied by the positive AHE becoming more pronounced with the decrease in temperature [28, 29]. The films studied in [28, 29] were grown by the pulsed laser deposition (PLD) technique using the “direct” geometry (DG films) where the active surface of a substrate faces the laser plume. In contrast to the films studied in [28, 29], the $\text{Mn}_x\text{Si}_{1-x}$ ($x \approx 0.51–0.52$) layers studied in the present work were grown by the PLD technique using the so-called shadow geometry (SG films) where Mn and Si atoms are deposited onto the active surface of the substrate after undergoing the collisions with atoms of the buffer gas [30]. In this case, we can achieve low energies of deposited atoms and, at the same time, high deposition rates. The studies of magnetic characteristics of the SG films [30] reveal the existence of two ferromagnetic phases, namely, the low-temperature (LT) phase with $T_C \approx 46$ K and the high-temperature (HT) phase with $T_C \approx 370$ K. They arise owing to the formation of two layers with quite different sizes of crystallites. In the present work, we study in detail the magnetotransport characteristics of the SG films. We find that these films, as well as the DG films [28, 29], exhibit a positive AHE at room temperature. On cooling, however, the AHE changes its sign at $T \approx 30–50$ K; this temperature value depends on the film thickness.

2. The SG $\text{Mn}_x\text{Si}_{1-x}$ film was prepared in the shadow geometry in the presence of Kr gas (at a pressure of about 0.01 mbar) by depositing onto a 10×15 -mm Al_2O_3 (0001) substrate using a stoichiometric MnSi target [30]. The substrate temperature (340°C) was kept the same as that in the case of producing the DG SG $\text{Mn}_x\text{Si}_{1-x}$ layers. However, in our case, the film growth rate was much higher (≥ 7 nm/min). To determine the film composition and its thickness, we employed Rutherford backscattering spectroscopy (RBS) [30]. The thickness d of the deposited film depends on the distance L from the target and decreases with the growth of L from $d \approx 270$ to 70 nm along the length $\delta L \approx 15$ mm of the Al_2O_3 substrate. Simultaneously, the Mn content grows from 0.506 to 0.517. With the decrease in d from 160 to 70 nm ($\delta L \approx 10$ mm), the film composition only slightly depends on L ($x \approx 0.514–0.517$).

The structural characteristics of the grown films were studied by X-ray diffraction analysis using a Rigaku SmartLab diffractometer and by transmission electron microscopy (TEM) and high-resolution transmission electron microscopy (STEM) using a

TITAN 80-300 microscope (FEI, United States) equipped with an image spherical aberration corrector in the bright- and dark-field modes. In the latter case, the scanning of the sample was performed using a high-angle annular dark-field (HAADF) detector of scattered electrons. The implementation of such a detector ensures obtaining images with the contrast depending on the number of the chemical element (Z contrast). The accelerating voltage was 300 kV. The image processing was performed using the Digital Micrograph program package (Gatan, United States).

For the transport and magnetic measurements, the $\text{Mn}_x\text{Si}_{1-x}/\text{Al}_2\text{O}_3$ large-area structure was cut into seven 2×10 -mm strips having different thicknesses of the $\text{Mn}_x\text{Si}_{1-x}$ films. The studies of the Hall effect were performed in the double Hall bar geometry using an evacuated insert with a superconducting solenoid in the temperature range of 5–100 K at the applied magnetic field up to 2.5 T [28, 29]. The contacts were prepared by indium soldering. The distance between the voltage probes at side faces of the sample was about 2.5 mm. The magnetization of 2×1.5 -mm samples was measured using an MPMS-3 magnetometer (SQUID-VSM) at fields up to 1.5 T in the temperature range of 5–400 K. The field was applied parallel to the sample surface. Below, we present the results of the transport and magnetic measurements for samples 1–4, corresponding to the largest distance from the target. They have close values of x ($x \approx 0.517, 0.516, 0.515$, and 0.514) and film thicknesses $d \approx 70, 90, 110$, and 160 nm, respectively.

3. In Fig. 1, we show the temperature dependence of the normalized resistivity $\rho(T)$ for samples 1 and 4 ($d \approx 70$ and 160 nm, respectively). For comparison, we also show the $\rho(T)$ plot for the MnSi single crystal with the B20-type structure (further on, ϵ -MnSi for brevity) taken from [31]. For both samples, the resistivity decreases on cooling. This decrease is steeper for the thicker film: $r(11.5 \text{ K}) = \rho(11.5 \text{ K})/\rho(290 \text{ K}) \approx 0.29$ and 0.21 ($\rho \approx 3.4 \times 10^{-5}$ and $2.75 \text{ } \Omega \text{ cm}$ at 11.5 K) for the samples with $d \approx 70$ and 160 nm, respectively. For ϵ -MnSi films, the decrease in the resistivity is larger by an order of magnitude ($r \approx 0.02$ [31]), whereas $\rho(T)$ has the same form as in our $\text{Mn}_x\text{Si}_{1-x}$ films (a steep decrease in $\rho(T)$ below about 30 K [31, 32]). Hence, the existence of the ϵ -MnSi type phase manifests itself in the samples under study. This fact is supported by the X-ray diffraction measurements of the $\text{Mn}_x\text{Si}_{1-x}/\text{Al}_2\text{O}_3(0001)$ structure before its cutting into separate strips (see inset in Fig. 1). The diffraction pattern exhibits more than four peaks. The most intense peak is observed at an angle $2\theta = 44.46^\circ$ corresponding to MnSi(210) for CuK_α radiation. At $2\theta = 44.46^\circ$, the full width at half maximum of the rocking curve (FWHM_ω) is about 550 arcsec, whereas the FWHM_ω for the single-crystalline film should vary from 64 to 245 arcsec with the change in the film thickness from 70 to 270 nm, respectively. Such a

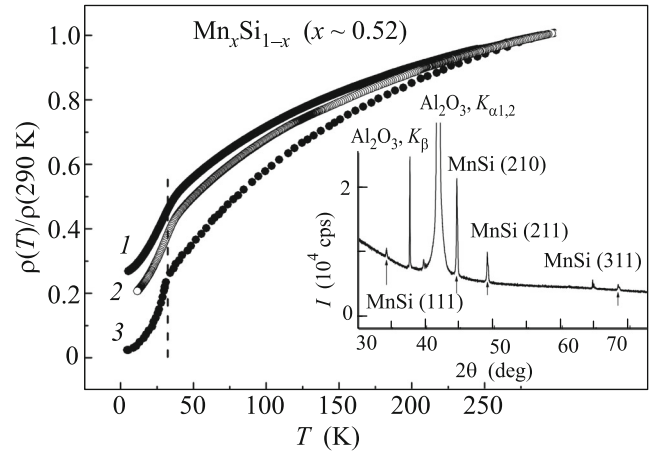


Fig. 1. Temperature dependence of the electrical resistivity $\rho(T)$ for the $\text{Mn}_x\text{Si}_{1-x}/\text{Al}_2\text{O}_3$ samples with $d \approx$ (1) 70 and (2) 160 nm, as well as (3) the $\rho(T)$ curve for ϵ -MnSi taken from [31]. The X-ray diffraction spectrum for the $\text{Mn}_x\text{Si}_{1-x}/\text{Al}_2\text{O}_3(0001)$ structure before its cutting into separate strips is shown in the inset.

broad peak is a signature of the pronounced mosaicity of the film under study and/or of a high content of crystal defects in it.

In Fig 2a, we demonstrate the bright-field TEM image of the $\text{Mn}_x\text{Si}_{1-x}/\text{Al}_2\text{O}_3(0001)$ structure with the thickness of the $\text{Mn}_x\text{Si}_{1-x}$ film $d \approx 250$ nm. We can see that the film as a whole can be treated as a layer consisting of columnar grains with a transverse size of about 50 nm. The detailed study of the interface between the columns and the Al_2O_3 substrate reveals thin interfacial spacers (see Fig. 2b), which are most clearly pronounced in the TEM images obtained in the dark-field mode (Fig. 2c). According to these studies, the thickness of the interfacial layer is about 7–10 nm.

The results of high-resolution TEM studies (Fig. 2d), including those based on Fourier analysis (Fig. 2e), unambiguously demonstrate that the columnar grains are formed by the ϵ -MnSi compound in agreement with the X-ray diffraction measurements. The analysis of the high-resolution TEM data shows that the interfacial layer consists of rounded grains 5–7 nm in diameter, which are also formed by the ϵ -MnSi silicide having the B20 structure. The formation of the interfacial layer is probably caused by the different symmetries of the α - Al_2O_3 substrate (hexagonal) and ϵ -MnSi (cubic) and the thus arising significant lattice mismatch (about 10% at the preferable [111] growth direction). (Estimating this mismatch, we take into account that the distance between the $\{1120\}_{\alpha\text{-Al}_2\text{O}_3}$ planes is $d = 2.38 \text{ } \text{Å}$ and that between $\{111\}_{\text{MnSi}}$ is $d = 2.63 \text{ } \text{Å}$.)

Since ϵ -MnSi is the dominant phase in the prepared $\text{Mn}_x\text{Si}_{1-x}$ film, the film should exhibit a nega-

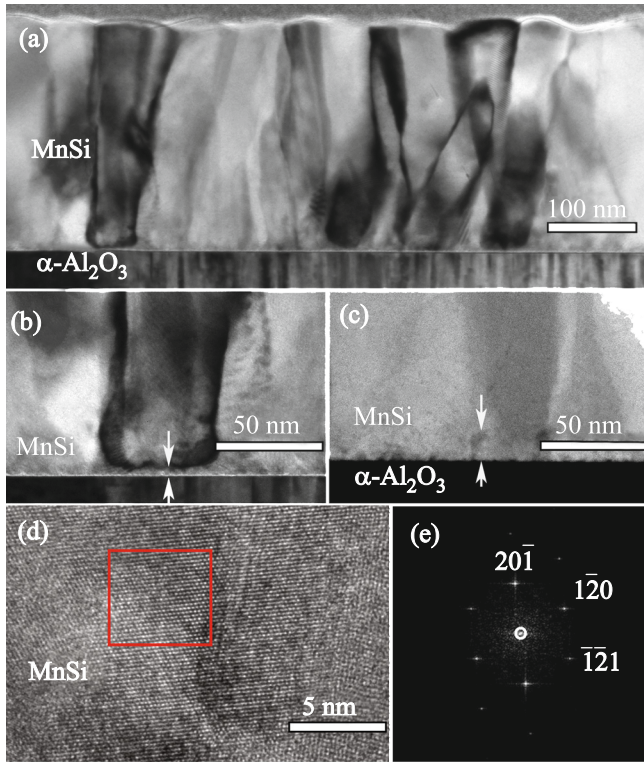


Fig. 2. (Color online) (a) Bright-field TEM image of the $\text{Mn}_x\text{Si}_{1-x}/\text{Al}_2\text{O}_3$ (0001) structure with the thickness $d \approx 250$ nm of the $\text{Mn}_x\text{Si}_{1-x}$ film. (b) Magnified TEM image of the interface; the arrows indicate the MnSi layer with a grain size of 5–10 nm. (c) Dark-field STEM image of the interface with detection of electrons scattered to large angles. (d) Bright-field TEM image of a columnar grain in the film with the resolution of the order of the lattice constant. The red square marks the portion of the sample used for obtaining (e) the two-dimensional Fourier spectrum characteristic of the B20 structure in the projection onto [214].

tive AHE [33]. For ϵ -MnSi, the absolute value of the Hall resistivity has a peak near the ferromagnetic transition ($|\rho_H^a| \approx 0.14 \mu\Omega \text{ cm}$ at $T_C \approx 30$ K) and decreases significantly at $T < T_C$ (down to $|\rho_H^a| \sim 0.01 \mu\Omega \text{ cm}$ at $T \approx 10$ K) [33, 34]. In our case, the behavior is radically different.

In Fig. 3a, we show the magnetic field dependence of the Hall resistivity $\rho_H(B)$ for sample 1 ($d \approx 70$ nm). We can see that the AHE has the positive sign, which is retained up to room temperature, similar to the situation characteristic of the DG $\text{Si}_{1-x}\text{Mn}_x$ ($x \approx 0.5$) films [28, 29]. In our case, however, the Hall resistivity decreases appreciably on cooling at temperatures below $T \approx 200$ K (by a factor of about 10 at $T = 5$ K), in contrast to the DG films, for which we have $\rho_H(B) \approx \text{const}$ in the temperature range of 5–200 K (see inset in Fig. 3a).

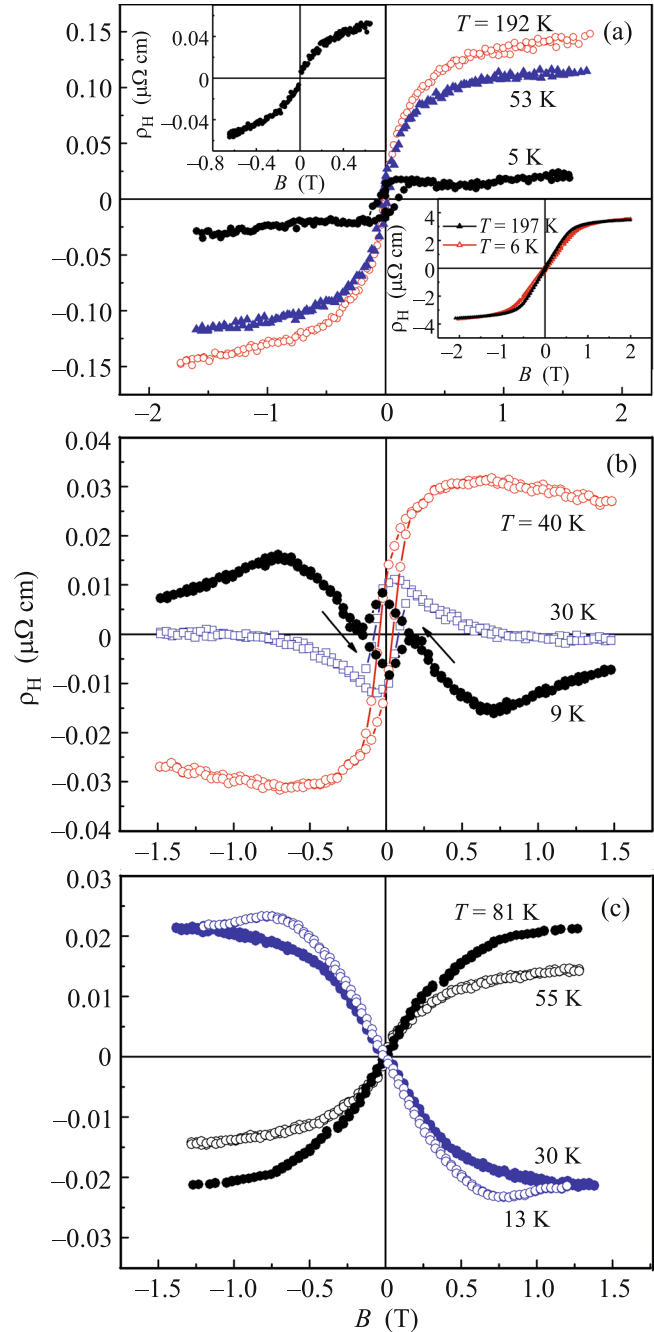


Fig. 3. (Color online) Magnetic-field dependence of the Hall resistivity $\rho_H(B)$ for the samples with $d \approx$ (a) 70, (b) 90, and (c) 110 nm measured at different temperatures. The upper inset in panel (a) shows the $\rho_H(B)$ curve at $T = 300$ K. The lower inset in panel (a) shows the $\rho_H(B)$ curves for the $\text{Mn}_x\text{Si}_{1-x}$ ($x \approx 0.52$) film prepared using the “direct” geometry in the PLD method.

The comparison of the $\rho_H(B)$ curves for sample 1 ($d \approx 70$ nm) and thicker sample 2 ($d \approx 90$ nm) shown in Fig. 3b clearly demonstrates that the AHE in this system includes the contributions of both positive and

negative components. The role of the latter grows with the film thickness especially at temperatures below 50 K. In particular, this manifests itself in the negative sign of the Hall effect in sample 2 at low temperatures ($T \leq 30$ K) and at the applied magnetic field $B \geq 1$ T (see Figs. 3b and 4). At $T = 9$ K, the hysteresis loop observed in the $\rho_H(B)$ curve exhibits a quite unusual shape (Fig. 3b). It is easy to show that such a shape of the hysteresis curve results from the superposition of two components involved in the AHE resistivity $\rho_H^a = R_s M$. One of them, $\rho_{H1}^a > 0$, exhibits a hysteresis, whereas the other one, $\rho_{H2}^a < 0$, has no hysteresis in its magnetic field dependence $\rho_{H2}^a(B)$, as in the case of helicoidal ϵ -MnSi [33, 34]. However, the latter component, which seems to be related to the sufficiently thick upper layer (Figs. 2a–2c), similar to ϵ -MnSi with a small negative AHE [33], makes the dominant contribution to the electrical conductivity of the sample. Note also that the normal Hall effect in ϵ -MnSi is positive [33, 34]. Therefore, it is not surprising that the linear form of $\rho_H(B)$ at the magnetic field $B \geq 0.7$ T corresponds to the hole conductivity (Fig. 3b).

Sample 3 with $d \approx 110$ nm no longer exhibits hysteresis on its $\rho_H(B)$ curves (Fig. 3c). In this case, the AHE has the negative sign at $T = 30$ K within the whole magnetic field range under study.

In Fig. 4, we show the temperature dependence $\rho_H(T)$ for samples 2–4 with different thickness of the $\text{Si}_{1-x}\text{Mn}_x$ film ($d \approx 90, 110,$ and 160 nm, respectively) measured at $B = 1.2$ T. The temperature corresponding to the change in the sign of the AHE T_{sc} increases with the film thickness from $T \approx 30$ K to ≈ 50 K. At $T > 50$ K, the Hall resistance for sample 4 ($d \approx 160$ nm) turns out to be rather low, $\rho_H \sim 0.01 \mu\Omega$, i.e., two orders of magnitude lower than that for the DG $\text{Si}_{1-x}\text{Mn}_x$ ($x \approx 0.5$) films (see the lower inset in Fig. 3a and [28, 29]). It is natural to attribute such behavior of T_{sc} with the growth of d to the increase in the contribution to the conductivity of the $\text{Si}_{1-x}\text{Mn}_x$ film coming from the upper ϵ -MnSi-type layer (with $\text{AHE} < 0$) at the fixed contribution from the lower (interfacial) layer. The latter is characterized by a significantly larger absolute value of the AHE than that of the upper layer. This is clearly seen at room temperature.

The measurements of the magnetization confirm that two ferromagnetic phases exist in the samples; the contribution of one of them to the magnetization J_m is independent of the thickness of the $\text{Si}_{1-x}\text{Mn}_x$ film. In Fig. 5a, we illustrate the temperature dependence of the surface magnetization density $J_m(T)/A$ (where A is the area of the structures under study) measured for $\text{Mn}_x\text{Si}_{1-x}$ samples 2 and 4 ($x \approx 0.516$ and 0.514 , respectively) with the film thickness $d \approx 90$ and 160 nm, respectively, at the field $\mu_0 H = 1$ T. The form of these curves suggests the existence of two magnetic

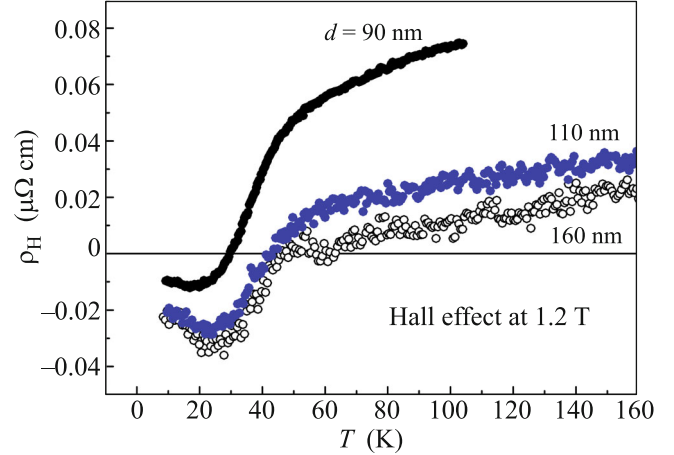


Fig. 4. (Color online) Temperature dependence of the Hall resistivity $\rho_H(T)$ measured at $B = 1.2$ T for samples 2–4 with different thicknesses of the $\text{Mn}_x\text{Si}_{1-x}$ film ($d = 90, 110,$ and 160 nm).

phases in the samples: the high-temperature ferromagnetic (HT FM) phase with $T_C \approx 340$ K and the low-temperature ferromagnetic (LT FM) phase with $T_C \approx 46$ K. The relative contribution of the latter increases with the film thickness, whereas the contribution of the HT FM phase remains nearly the same. Hence, the HT FM phase is formed directly at the Al_2O_3 (0001) substrate, and after that, the formation of the LT FM phase ($T_C \approx 46$ K) of the ϵ -MnSi type occurs. Note that the saturation magnetization is $M_s \approx 190$ emu/cm³ in the thick film ($d \approx 160$ nm) at $T \approx 4$ K (see inset in Fig. 5a). This value is several times smaller than that for the DG $\text{Mn}_x\text{Si}_{1-x}$ film with $x \approx 0.52$ [30] and close to $M_s \approx 146$ emu/cm³ characteristic of ϵ -MnSi [31].

In Fig. 5b, we show the temperature dependence of magnetization for samples 1 ($x \approx 0.517, d \approx 90$ nm) and 4 ($x \approx 0.514, d \approx 160$ nm) measured on heating at the low applied field of 10 mT after the zero field cooling (ZFC curves). We also show for comparison the $J_m(T)$ curve for sample 1 obtained after its cooling at a field of 1 T (FC curve). The manifestation of two peaks on the ZFC curves is a signature of the block-type (polycrystalline) structure of the system and the existence of HT and LT FM phases. Note that the positions of the peaks are independent of the film thickness, suggesting that the magnetic structure of SG films depends only slightly on their thickness.

4. The structural TEM data presented above clearly demonstrate that the samples contain the layer formed by columnar ϵ -MnSi grains with a size of about 50 nm in the film plane having the B20-type structure (Fig. 2). It is well known that ϵ -MnSi single crystals are characterized by a negative AHE and have $T_C \approx 30$ K [33, 34]. Moreover, the TEM studies show the

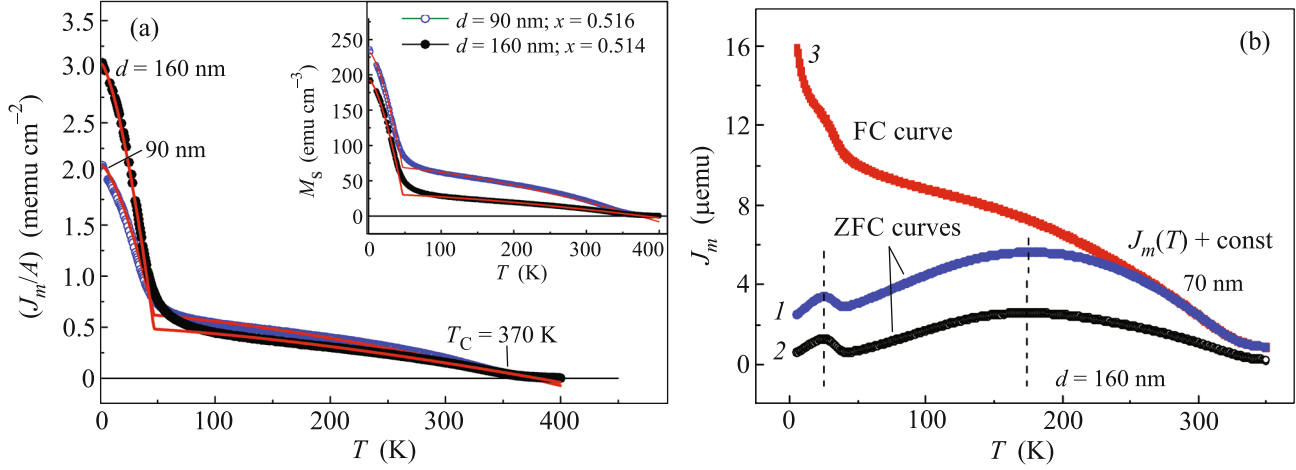


Fig. 5. (Color online) (a) Temperature dependence of the surface magnetization density $J_m(T)/A$ (A is the area of the structure) measured in the field $\mu_0 H = 1$ T for $\text{Mn}_x\text{Si}_{1-x}$ samples 2 and 4 with the film thicknesses $d \approx 90$ and 160 nm, respectively. The inset demonstrates the corresponding temperature dependence of the saturation magnetization $M_s(T)$ for these samples. (b) $J_m(T)$ curves for (1) sample 1 with $d \approx 90$ nm and (2) sample 4 with $d \approx 160$ nm measured at heating in the low applied magnetic field of 10 mT after the zero-field cooling (ZFC) and (3) the $J_m(T)$ curve for sample 1 at 10 mT obtained after its cooling in a field of 1 T (FC). For convenience, curves 1 and 3 are shifted along the vertical axis by a certain constant.

existence of an interfacial layer with a thickness of about 10 nm located at the Al_2O_3 substrate. This layer consists of small rounded grains (~ 5 nm in size). The magnetic and transport measurements certainly indicate that just this interfacial layer is responsible for the HT FM phase accompanied by the pronounced positive AHE. The results of TEM studies do not show the existence of a sharp boundary between the HT and LT FM layers. Nevertheless, this does not prevent the formation of the continuous conducting channel in the interfacial layer characterized by the positive AHE. Taking into account the results of the structural studies, we analyze below the transport and magnetic data using the two-layer model.

First, let us estimate the magnetic moment per Mn atom in the layers, assuming that the interfacial layer thickness is about 10 nm and the density of the non-stoichiometric $\text{Mn}_x\text{Si}_{1-x}$ ($x \sim 0.52$) film is about 5.82 g/cm³ as in bulk ϵ -MnSi. We find the contributions of the HT and LT FM layers to the magnetization by approximating the temperature dependence of the saturation magnetization $M_s(T)$ by the often used simplified Brillouin function

$$M_s(T) = M_s(0)[1 - (T/T_C)^n]. \quad (2)$$

In our case, relation (2) with $n = 1.5$ fits well the experimental $M_s(T)$ curves (see Fig. 5a). Using the contributions of the HT FM and LT FM phases calculated by Eq. (2), we obtain the magnetic moments $m = 1.3$ – 1.75 and 0.43 – 0.52 μ_B/Mn , respectively, at $x \approx 0.514$ – 0.517 . The magnetic moment $m = 0.43$ – 0.52 μ_B/Mn for the LT FM phase agrees well with the effective magnetic moment of Mn in the ϵ -MnSi lattice ($m \approx$

0.4 μ_B/Mn) [31, 33]. Here, we should take into account that the LT FM layer contains excess Mn ions, which promote the formation of defects with the localized magnetic moments (up to about 2 μ_B/Mn at $x \sim 0.51$ [29]). Note also that the magnetic moment corresponding to the HT FM layer, $m = 1.3$ – 1.75 μ_B/Mn , is somehow higher than that for DG $\text{Mn}_x\text{Si}_{1-x}$ films ($x \approx 0.52$) with $T_C \approx 330$ K, where $m = 1.1$ μ_B/Mn [28].

Let us now analyze the transport data taking into account a certain similarity between the interfacial layer and the DG films studied in [28, 29]. For two parallel conducting layers, the effective Hall resistivity of the film is determined by the expression [35]

$$R_H = \frac{\rho_{H2}\sigma_2^2 d_2 + \rho_{H1}\sigma_1^2 d_1}{(\sigma_1 d_1 + \sigma_2 d_2)^2}, \quad (3)$$

where subscripts 1 and 2 correspond to the lower (HT FM) and upper (LT FM) layers, respectively. It follows from Eq. (3) that we can expect the change in sign of the Hall effect for thick films ($d \sim d_2 \gg d_1$). Indeed, at temperatures below $T_C \approx 46$ K, the anomalous contribution to the Hall effect having the negative sign ($\rho_{H2}^a < 0$) begins to play the dominant role [33].

We assume that the AHE resistivity of the lower layer is $\rho_{H1}^a \approx +3.5 \times 10^{-6}$ Ω cm at $T < 200$ K as in the DG films [28] and the AHE resistivity of the upper layer is $\rho_{H2}^a \approx -(0.1$ – $0.2) \times 10^{-6}$ Ω cm at $T = 25$ – 40 K as that for ϵ -MnSi [33, 34]. Then, taking into account that the change in the sign of the Hall effect is observed at the film thickness $d = d_2 + d_1 \approx 70$ – 90 nm (see

Fig. 3), we find that the ratio of conductivities of the layers is $\sigma_2/\sigma_1 \sim 2$. In other words, although the size of crystallites in the lower layer is much smaller (by a factor of 10 or more) than that in the upper layer, the difference of their conductivities at low temperatures is not so large. We apparently observe the same effect as in the DG films, where the formation of magnetic defects is accompanied by a nearly tenfold increase in the mobility of charge carriers at $T \sim 100$ K in comparison to the value characteristic of ϵ -MnSi. In [28], such a behavior is attributed to the destruction of collective (Kondo or spin-polaron) resonances.

5. Finally, let us discuss the characteristic features of the physical mechanism underlying the HT FM phase in the SG films. The HT FM phase, which we earlier observed in nonstoichiometric $\text{Mn}_x\text{Si}_{1-x}$ ($x \approx 0.52-0.55$) alloys [28, 29], was attributed to the formation of defects with the localized magnetic moments (LMMs) and to the indirect exchange interaction between LMMs by means of the paramagnetic spin density fluctuations in the framework of the model proposed in [36]. According to the TEM and the Rutherford backscattering data [30], Mn is uniformly distributed over the thickness of SG $\text{Mn}_x\text{Si}_{1-x}$ films. At first glance, the physical mechanism of the HT FM discussed in [28] does not work in the case of SG films. Indeed, as was shown in [28], the favorable conditions for the formation of LMM arise only if the excess of Mn in the films is accompanied by the formation of Si vacancies in them. Only in this case, the LMMs can be large (up to $m = 2.58 \mu_B$ at $x \approx 0.52$). If a Mn ion occupies an interstitial position in the crystal lattice, it turns out to be “magnetically dead” ($m = 0.09 \mu_B$ at $x \approx 0.52$). Therefore, if we assume that the excess Mn in the layer consisting of columnar grains with a “large” (~ 50 nm) transverse size is due mostly to the interstitial Mn ions, the aforementioned contradiction is removed. Indeed, in the interfacial layer, with small (~ 5 nm) grain size, we should expect the effective gettering of Mn defects at the grain boundaries accompanied by a significant increase in the magnitude of LMMs at these boundaries (see [36] and references therein). Probably, the shape of grains plays an important role in the formation of defects with LMMs at the grain boundaries. For example, in the recent study of dilute $\text{Mn}_x\text{Si}_{1-x}$ ($x < 0.04$) alloys, it was found that the Mn-enriched precipitates grown in the shape of transverse nanocolumns are paramagnets, whereas the precipitates in the shape of “planar bars” exhibit ferromagnetic properties up to room temperature [37]. At the inhomogeneous distribution of LMMs over the grain boundaries, the global ferromagnetic order can be described in terms of the model proposed in [36], where the grain radii are $r_0 \ll \zeta$, where ζ is the FM correlation length. Estimates show that the HT FM phase with $T_C \sim 100-400$ K can exist in our case at small grain sizes (~ 5 nm).

In conclusion, the experimental data discussed above have demonstrated that the structural features of polycrystalline $\text{Mn}_x\text{Si}_{1-x}$ ($x \approx 0.5$) films completely determine the behavior of the anomalous Hall effect in them, in particular, the change in the sign of the AHE with the decrease in temperature. It has been shown that the change in the sign of the AHE is caused by the competition of two contributions coming from different parts of the sample (interfacial and bulk), in contrast to other works where the change in the sign is attributed either to the specific features of the electron density of states at the Fermi level and with the change in its position with temperature [5, 25, 26] or to the competition of the temperature-dependent mechanisms determining the sign of the AHE [10, 11, 24].

This work was supported in part by the Russian Science Foundation (project no. 16-19-10233), in part by the Russian Foundation for Basic Research (project nos. 14-07-91332, 14-22-01063, 14-07-00688, 14-47-03605, 15-07-01160, 15-02-02077, 16-07-00657, and 16-07-00798), and by Deutsche Forschungsgemeinschaft (DFG, grant no. ZH 225/6-1).

REFERENCES

1. R. Karplus and J. M. Luttinger, *Phys. Rev.* **95**, 1154 (1954).
2. N. Nagaosa, J. Sinova, S. Onoda, A. H. MacDonald, and N. P. Ong, *Rev. Mod. Phys.* **82**, 1539 (2010).
3. S. N. Nikolaev, B. A. Aronzon, V. V. Ryl'kov, V. V. Tugushev, E. S. Demidov, V. P. Lesnikov, and V. V. Podol'skii, *JETP Lett.* **89**, 603 (2009).
4. Y. Tian, L. Ye, and X. Jin, *Phys. Rev. Lett.* **103**, 087206 (2009).
5. D. Chiba, A. Werpachowska, M. Endo, Y. Nishitani, F. Matsukura, T. Dietl, and H. Ohno, *Phys. Rev. Lett.* **104**, 106601 (2010).
6. X. Liu, S. Shen, Z. Ge, W. L. Lim, M. Dobrowolska, and J. K. Furdyna, *Phys. Rev. B* **83**, 144421 (2011).
7. A. Shitade and N. Nagaosa, *J. Phys. Soc. Jpn.* **81**, 083704 (2012).
8. Yu. A. Mikhailovskii, D. E. Mettus, A. P. Kazakov, V. N. Prudnikov, Yu. E. Kalinin, A. S. Sitnikov, A. Gerber, D. Bartov, and A. B. Granovskii, *JETP Lett.* **97**, 473 (2013).
9. D. Bartov, A. Segal, M. Karpovski, and A. Gerber, *Phys. Rev. B* **90**, 144423 (2014).
10. L. N. Oveshnikov, V. A. Kul'bachinskii, A. B. Davydov, and B. A. Aronzon, *JETP Lett.* **100**, 570 (2014).
11. S. A. Meynell, M. N. Wilson, J. C. Loudon, A. Spitzig, F. N. Rybakov, M. B. Johnson, and T. L. Monchesky, *Phys. Rev. B* **90**, 224419 (2014).
12. Yu. O. Mikhailovsky, V. N. Prudnikov, K. Yu. Chernoglazov, V. V. Ryl'kov, S. N. Nikolaev, A. V. Sitnikov, Yu. E. Kalinin, D. Bartov, A. Gerber, and A. B. Granovsky, *Solid. State Phenom.* **233-234**, 403 (2015).
13. D. Hou, G. Su, Y. Tian, X. Jin, S. A. Yang, and Q. Niu, *Phys. Rev. Lett.* **114**, 217203 (2015).
14. A. V. Ved'yayev, N. V. Ryzhanova, N. Strelkov, and B. Dieny, *Phys. Rev. Lett.* **110**, 247204 (2013).

15. J. Smit, *Physica* **21**, 877 (1955).
16. L. Berger, *Phys. Rev. B* **2**, 4559 (1970).
17. T. Jungwirth, Q. Niu, and A. H. MacDonald, *Phys. Rev. Lett.* **88**, 207208 (2002).
18. M. Onoda and N. Nagaosa, *J. Phys. Soc. Jpn.* **71**, 19 (2002).
19. T. Fukumura, H. Toyosaki, K. Ueno, M. Nakano, T. Yamasaki, and M. Kawasaki, *Jpn. J. Appl. Phys.* **46**, L642 (2007).
20. A. Fernández-Pacheco, J. M. De Teresa, J. Orna, L. Morellon, P. A. Algarabel, J. A. Pardo, and M. R. Ibarra, *Phys. Rev. B* **77**, 100403(R) (2008).
21. M. Glunk, J. Daeubler, W. Schoch, R. Sauer, and W. Limmer, *Phys. Rev. B* **80**, 125204 (2009).
22. B. A. Aronzon, D. Yu. Kovalev, A. N. Lagar'kov, E. Z. Meilikhov, V. V. Ryl'kov, M. V. Sedova, N. Negre, M. Goiran, and J. Leotin, *JETP Lett.* **70**, 90 (1999).
23. S. Onoda, N. Sugimoto, and N. Nagaosa, *Phys. Rev. Lett.* **97**, 126602 (2006), *Phys. Rev. B* **77**, 165103 (2008).
24. J. G. Checkelsky, M. Lee, E. Morosan, R. J. Cava, and N. P. Ong, *Phys. Rev. B* **77**, 014433 (2008).
25. Z. Fang, N. Nagaosa, K. S. Takahashi, A. Asamitsu, R. Mathieu, T. Ogasawara, H. Yamada, M. Kawasaki, Y. Tokura, and K. Terakura, *Science* **302**, 92 (2003).
26. M. Eginligil, G. Kim, Y. Yoon, J. P. Bird, H. Luo, and B. D. McCombe, *Physica E* **40**, 2104 (2008).
27. A. V. Vedyayev, A. B. Granovskii, and O. A. Kotel'nikova, *Kinetic Phenomena in Disordered Ferromagnetic Alloys* (Mosk. Gos. Univ., Moscow, 1992) [in Russian].
28. V. V. Ryl'kov, S. N. Nikolaev, K. Yu. Chernoglazov, B. A. Aronzon, K. I. Maslakov, V. V. Tugushev, E. T. Kulatov, I. A. Likhachev, E. M. Pashaev, A. S. Semisalova, N. S. Perov, A. B. Granovskii, E. A. Gan'shina, O. A. Novodvorskii, O. D. Khramova, E. V. Khaidukov, and V. Ya. Panchenko, *JETP Lett.* **96**, 255 (2012).
29. V. V. Rylkov, E. A. Gan'shina, O. A. Novodvorskii, S. N. Nikolaev, A. I. Novikov, E. T. Kulatov, V. V. Tugushev, A. B. Granovskii, and V. Ya. Panchenko, *Europhys. Lett.* **103**, 57014 (2013).
30. S. N. Nikolaev, A. S. Semisalova, V. V. Rylkov, V. V. Tugushev, A. V. Zenkevich, A. L. Vasiliev, E. M. Pashaev, K. Yu. Chernoglazov, Yu. M. Chesnokov, I. A. Likhachev, N. S. Perov, Yu. A. Matveyev, O. A. Novodvorskii, E. T. Kulatov, A. S. Bugaev, Y. Wang, and S. Zhou, *AIP Adv.* **6**, 015020 (2016).
31. S. V. Demishev, V. V. Glushkov, I. I. Lobanova, M. A. Anisimov, V. Yu. Ivanov, T. V. Ishchenko, M. S. Karasev, N. A. Samarin, N. E. Sluchanko, V. M. Zimin, and A. V. Semeno, *Phys. Rev. B* **85**, 045131 (2012).
32. F. P. Mena, D. van der Marel, A. Damascelli, M. Fath, A. A. Menovsky, and J. A. Mydosh, *Phys. Rev. B* **67**, 241101(R) (2003).
33. M. Lee, Y. Onose, Y. Tokura, and N. P. Ong, *Phys. Rev. B* **75**, 172403 (2007).
34. A. Neubauer, C. Pfleiderer, R. Ritz, P. G. Niklowitz, and P. Boni, *Physica B* **404**, 3163 (2009).
35. E. V. Kuchis, *Halvanomagnetic Effects and Methods of Their Investigations* (Radio Svyaz', Moscow, 1990) [in Russian].
36. V. N. Men'shov, V. V. Tugushev, S. Caprara, and E. V. Chulkov, *Phys. Rev. B* **83**, 035201 (2011).
37. S. Kahwaji, W. Bowman, M. D. Robertson, and T. L. Monchesky, *J. Appl. Phys.* **113**, 063910 (2013).

Translated by K. Kugel